CHEMISTRY OF MATERIALS

Article

pubs.acs.org/cm

# Integration of Upconversion Nanoparticles and Ultrathin Black Phosphorus for Efficient Photodynamic Theranostics under 808 nm Near-Infrared Light Irradiation

Ruichan Lv,[†] Dan Yang,[†] Piaoping Yang,*[,†] Jiating Xu,[†] Fei He,[†] Shili Gai,[†] Chunxia Li,[‡] Yunlu Dai,[†] Guixin Yang,[†] and Jun Lin*[,‡]

[†]Key Laboratory of Superlight Materials and Surface Technology, Ministry of Education, College of Material Sciences and Chemical Engineering, Harbin Engineering University, Harbin 150001, P. R. China

[‡]State Key Laboratory of Rare Earth Resource Utilization, Changchun Institute of Applied Chemistry, Chinese Academy of Sciences, Changchun 130022, P. R. China

Supporting Information

**ABSTRACT:** A proper photosensitizer and increased penetration depth are still two major challenges in photodynamic therapy (PDT). The conventional ultraviolet/visible irradiation light has low tissue penetration, which thus limits its clinical application. Herein, we for the first time designed a novel multifunctional composite by integrating $NaGdF_4$:Yb,Er@Yb@Nd@Yb upconversion nanoparticles (UCNPs) and black phosphorus sheets (BPS) for a single 808 nm laser light-mediated PDT. UCNPs, which served as the energy donor, were modified with poly(acrylic acid), and the BPS were stabilized by the PEG-$NH_2$; then the two counterparts were integrated into the UCNPs−BPS composite via electrostatic interaction. Under 808 nm near-infrared light irradiation, the composite exhibits excellent antitumor efficiency because of the large amount of reactive oxygen species generated compared with those under 650 and 980 nm irradiations with the same pump power, which has evidently been confirmed by *in vitro* and *in vivo* results. In particular, our work may pave the way for the wide application of black phosphorus-based materials in theranostics.

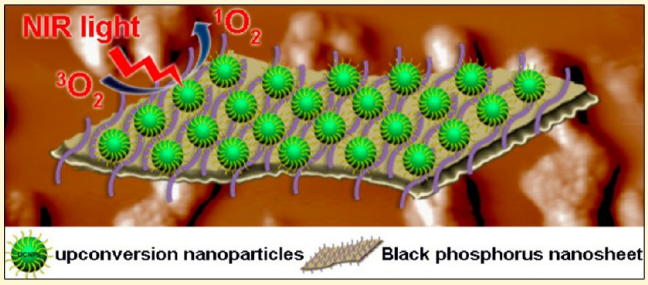


## INTRODUCTION

Photodynamic therapy (PDT) with unique advantages and low systematic toxicity has been proposed as a relatively less invasive tool, widely applied in the anticancer therapy and nanomedicine fields.[1−11] Three essential components of PDT treatments are a photosensitizer, reactive oxygen species (ROS), and irradiation light.[12−14] The conventionally used organic photosensitizers exhibit poor water solubility, low stability and quantum yield, and other ambiguous security issues.[15−17] The semiconductors and photocatalyst have been proposed as new PDT agents, which can be responsive to a broad range of wavelengths from ultraviolet to visible light.[18−22] Black phosphorus (BP), as the most stable allotrope of phosphorus, is being increasingly utilized as a metal-free semiconductor with an adjustable band gap through controlling the structure.[23−28] The thin black phosphorus sheets (BPS) could be produced in high yields using the liquid-phase exfoliation by breaking down the interlayer van der Waals forces.[29−32] Recently, Xie's group reported that the black phosphorus nanosheets with a high quantum yield could be an effective PDT agent.[33] However, despite the fact that the ultrathin BPS could be used as a potential therapeutic material, the irradiation wavelength located in the visible light region creates strong tissue interference, which greatly hinders its actual biomedical applications because of the limited penetration depth. Furthermore, the designed system has seen limited clinical use because of the lack of diagnostic function. To the best of our knowledge, there have been few reports of the utilization of black phosphorus (nanosheets, nanodots, etc.)-based materials in theranostics.[34] Moreover, when the therapy and diagnosis are performed under the same conditions, the two usually required light sources are difficult for real-time diagnostic application.[35−37] Thus, the design of a multifunctional composite to achieve the therapeutic and diagnostic functions upon a single light irradiation will be highly desirable.[38−40]

Upconversion luminescent (UCL) materials could modify the near-infrared (NIR) irradiation to visible light through a multiple-photon process, which has been extensively applied in imaging, antitumor therapy, and drug delivery fields.[41−52] However, the overlay of the absorbance of water in the body with the commonly used 980 nm laser irradiation gives rise to a

Received: April 28, 2016
Revised: June 15, 2016
Published: June 15, 2016





DOI: 10.1021/acs.chemmater.6b01720
Chem. Mater. 2016, 28, 4724−4734

high absorbance of light, leading to a small penetration depth and possible hyperthermia-induced tissue damage. Thus, shifting the wavelength of the irradiated light to an optical window (700−900 nm) that includes the minimal absorbance for biomolecules is necessary. Recently, the $Nd^{3+}$-sensitized UCL materials have been proposed using 808 nm NIR laser light as the irradiation source, which is located in the optical window with a large high penetration depth.[53−62] Just recently, our group proposed a facile and general route for preparing 808 nm light-excited core−shell structured UCNPs, and the obtained structure with the active shell has high UCL emission in the visible range, which is an advantage for diagnosis.[63,64] It is thus envisioned that when the UCNPs are combined with BPS, the irradiation laser light can be utilized to motivate the BPS and the generated emission can be used as an imaging probe to track the platform, processes that were mediated by a single irradiation source.

Herein, to achieve the 808 nm NIR light-mediated photodynamic therapy, we for the first time designed and fabricated a novel UCNP−BPS composite by integrating the ultrathin BPS with the small $NaGdF_4$:Yb,Er@Yb@Nd@Yb UCNPs. The UCNPs were modified with PAA first, and the BPS were stabilized by PEG-$NH_2$; then the two materials were integrated by electrostatic interaction. The efficiency of generated ROS was measured with different 650, 808, and 980 nm laser sources with the same pump power for comparison. The *in vitro* and *in vivo* experiments were also performed to examine the cancer inhibition efficacy.

## EXPERIMENTAL SECTION

**Reagents and Materials.** All the chemical reagents used were analytical grade without any further purification, including $Gd_2O_3$, $Yb_2O_3$, $Er_2O_3$, and $Nd_2O_3$ (99.99%) (from Sinopharm Chemical Reagent Co., Ltd., Shanghai, China), cyclohexane, *n*-hexane, and *n*-methyl-2-pyrrolidinone (NMP) (from Tianjin Kermel Chemical Reagent Co., Ltd., Tianjin, China), and oleic acid (OA), 1-octadecene (ODE), polyacrylic acid (PAA, 1800 $M_W$), PEG-$NH_2$, 1-[3-(dimethylamino)propyl]-3-ethylcarbodiimide hydrochloride (EDC), *N*-hydroxysuccinimide (NHS), 3-4,5-dimethylthiazol-2-yl-2,5-diphenyltetrazolium bromide (MTT), glutaraldehyde, 4′,6-diamidino-2-phenylindole (DAPI), calcein AM, and propidium iodide (PI) (from Sigma-Aldrich). Peptide $NH_2$-Gly-Arg-Gly-Asp-Ser (denoted as RGD) was synthesized by Sangon Biotechnology Co. Ltd. (Shanghai, China). Bulk black phosphorus (BP) was purchased from Nanjing XFNANO Materials Tech Co., Ltd.

**Preparation of Amino-Modified BPS.** The ultrathin black phosphorus nanosheets were prepared by liquid exfoliation of bulk black phosphorus according to the reported literature with some modification.[29] Briefly, 20 mg of bulk BP was first ground by hand and then dispersed in the mixture of 20 mL of the mixed solution of NMP, HCl, and deionized water (2:1:1 volume ratio) under vacuum with an ice/water bath for 8 h. Note that the ice/water bath was needed to prevent oxidation. Then, the suspension was kept for further use after being shaken softly and held in place. After that, the brown suspension was kept under 2000 rpm centrifugation for 5 min once to remove the unexfoliated bulk BP. The suspension was further centrifuged with deionized water for 5 min at 8000 rpm, and the precipitate was kept. For amino modification, the brown powder was dispersed into deionized water with 20 mg of PEG-$NH_2$ (dissolved into a water solution before immediate use) and stirred for 4 h under an ice/water bath. Finally, the solution was centrifuged three times with deionized water to remove surplus PEG-$NH_2$ and kept in cold storage for further use.

**Synthesis of OA-Coated $NaGdF_4$:Yb,Er.** OA-capped $NaGdF_4$:Yb,Er was synthesized by the developed route. In a typical route, 1 mmol of $RE(OA)_3$ (RE = 80% Gd, 19% Yb, and 1% Er), 12 mmol of NaF, and 30 mL of an oleic acid (OA)/1-octadecene (ODE) (1:1 volume ratio) mixed solvent were added to the reaction vessel and heated to 110 °C under vacuum for 30 min to remove residual oxygen and water. Subsequently, the temperature was increased to 300 °C, and the sample was held for 1.5 h under a $N_2$ atmosphere. The $NaGdF_4$:Yb,Er nanoparticles were obtained after being washed several times with ethanol and cyclohexane and dispersed in cyclohexane.

**Synthesis of $NaGdF_4$:Yb,Er@Yb@Nd@Yb.** The cyclohexane solution containing $NaGdF_4$:Yb,Er nanoparticles was added to a three-neck reaction vessel with 30 mL of OA/ODE (1:1 volume ratio), $Gd(CF_3COO)_3$ (0.45 mmol), $Yb(CF_3COO)_3$ (0.05 mmol), and $CF_3COONa$ (0.5 mmol) together. The solvent was heated to 120 °C under vacuum for 1 h and flushed with $N_2$. Then, the temperature was increased to 310 °C, and the sample was held for 1 h under a $N_2$ atmosphere. After that, the solution was cooled to room temperature to make the $NaGdF_4$:Yb,Er@$NaGdF_4$:Yb (denoted as $NaGdF_4$:Yb,Er@Yb) for further crystallization. The method for synthesis of the third shell of $NaGdF_4$:Yb,Er@$NaGdF_4$:Yb@$NaNdF_4$:Yb (denoted as $NaGdF_4$:Yb,Er@Yb@Nd) is similar, with the change of $Nd(CF_3COO)_3$ (0.45 mmol) and $Yb(CF_3COO)_3$ (0.05 mmol). For the fourth shell of $NaGdF_4$:Yb,Er@$NaGdF_4$:Yb@$NaNdF_4$:Yb@$NaGdF_4$:Yb (denoted as $NaGdF_4$:Yb,Er@Yb@Nd@Yb) nanoparticles, the amounts of $Gd(CF_3COO)_3$ (0.45 mmol) and $Yb(CF_3COO)_3$ (0.05 mmol) changed. After that, the final $NaGdF_4$:Yb,Er@Yb@Nd@Yb nanoparticles that were denoted as UCNPs were achieved. The sample was dispersed into 5 mL of cyclohexane for further use.

**Synthesis of UCNPs−PAA.** PAA powder (0.3 g) was dissolved in 15 mL of deionized water with ultrasonication, and then the solution was mixed with the as-synthesized $NaGdF_4$:Yb,Er@Yb@Nd@Yb (UCNPs) in cyclohexane. After the sample had been stirred for 6 h, there is no separated layer, and the water-soluble UCNPs−PAA was obtained after centrifugation.

**Synthesis of UCNPs−BPS.** UCNPs−PAA could be conjugated with BPS through electrostatic adsorption. Briefly, 10 mL of the as-prepared BPS, 1 mL of EDC (6 mg $mL^{-1}$), and 1 mL of NHS (2 mg $mL^{-1}$) were added and mixed with the as-prepared UCNPs−PAA in 30 mL of deionized water while being continuously stirred. After being stirred for 6 h, the UCNPs−BPS were obtained via centrifugation and dried at room temperature. Before the *in vitro* and *in vivo* experiment, the RGD peptide was first modified. Typically, 30 mg of UCNPs−BPS was mixed with 3 mg of RGD peptide in 30 mL of PBS. Three milliliters of EDC (6 mg $mL^{-1}$) and 3 mL of NHS (2 mg $mL^{-1}$) were added for better conjunction. After being stirred for 4 h, UCNPs−BPS with modified RGD were prepared.

**ROS Detection of UCNPs−BPS.** DPBF was employed as a chemical probe to determine singlet oxygen by measuring the absorption via UV−vis spectroscopy. Typically, 1 mL of an ethanol solution containing DPBF (1 mg $mL^{-1}$) was mixed with 1 mL of a UCNPs−BPS solution (1 mg $mL^{-1}$) and put into the 24-well plate. The solution was kept in the dark and irradiated with 650, 808, and 980 nm lasers (pump power of 1.44 W $cm^{-2}$) for different periods of time (0, 2, 5, 10, and 20 min). Then, the solution was centrifuged at 5000 rpm, and the supernatant was collected for UV−vis detection.

The intracellular ROS assay was conducted using DCFH-DA. HeLa cells were incubated in the six-well plate together with the coverslips. After the monolayer cells were obtained, a 1 mg $mL^{-1}$ UCNPs−BPS solution was added. After incubation for an additional 3 h, DCFH-DA was added and incubated for 10 min and then rinsed three times with PBS. After that, the cells were irradiated with different lasers with wavelengths of 650, 808, and 980 nm for 5 min. All the pump powers were 1.44 W $cm^{-2}$. The blank well without irradiation was also detected as the control. The fluorescence images were recorded at an irradiation wavelength of 488 nm.

***In Vitro* Cellular Uptake.** The cellular uptake by HeLa cell lines was studied with a confocal laser scanning microscope. Briefly, the cells were cultured with coverslips to obtain a monolayer in the six-well plates. Then, the cells were incubated with UCNPs−BPS at 37 °C for different periods of time. The cells were washed with PBS and fixed with 1 mL of 2.5% glutaraldehyde for 10 min. After a further rinse with





DOI: 10.1021/acs.chemmater.6b01720
*Chem. Mater.* 2016, 28, 4724−4734

**Scheme 1. Diagram of the Synthesis of UCNPs−BPS**

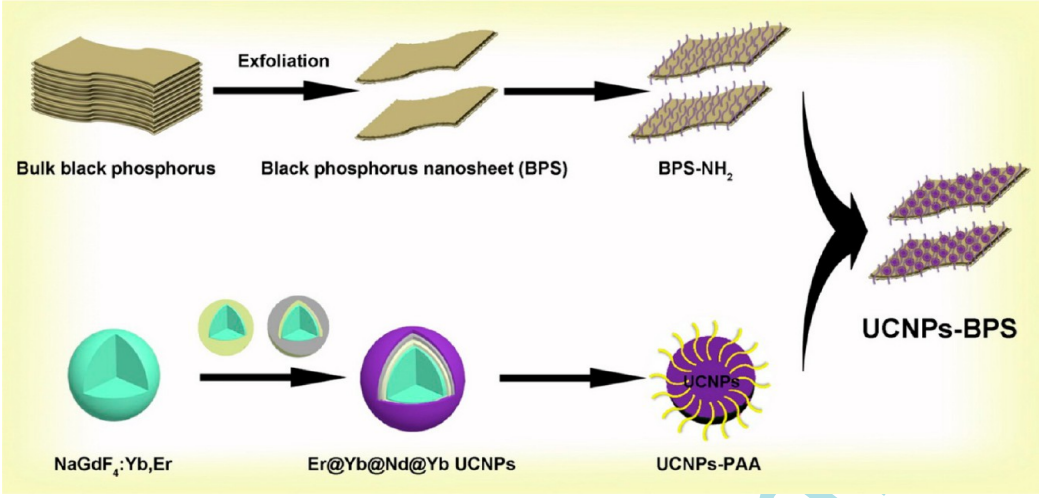


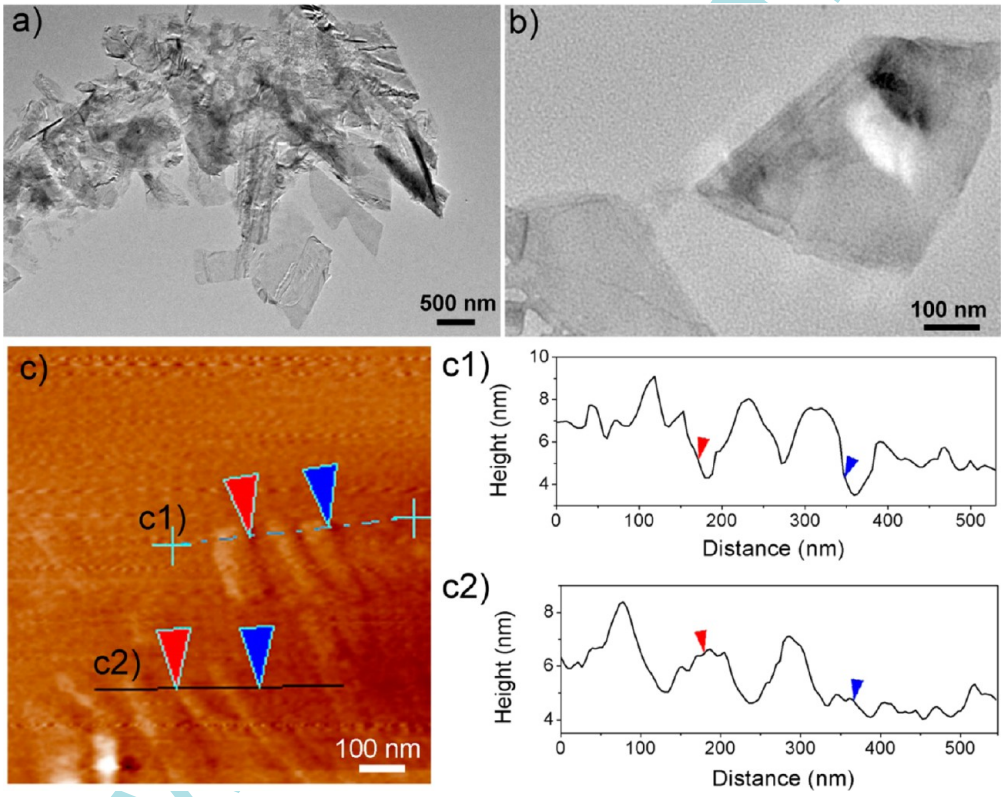


**Figure 1.** (a and b) TEM images of BPS. (c) AFM image and height profiles along the black lines of BPS.

PBS, the cells were stained with a 5 $\mu$g mL$^{-1}$ DAPI solution for an additional 10 min.

***In Vitro* Cytotoxicity Using the MTT Assay and Live/Dead State Detection.** The cell viability of the HeLa cells incubated with and without UCNPs−BPS was detected using the MTT assay and calcein AM/PI. The viability using the MTT assay was determined in a 96-well plate. Typically, the cells were incubated to obtain monolayer cells, and then UCNPs−BPS samples at different concentrations (500, 250, 125, 62.5, 31.3, and 15.6 $\mu$g mL$^{-1}$) were added to the three groups. After an additional 24 h, there different treatments (without irradiation and with 650 and 808 nm irradiation) were performed for 10 min. Both of the pump powers were 1.44 W cm$^{-2}$. Twenty microliters of the MTT solution (5 mg mL$^{-1}$) was added to each well, and the plate was incubated for an additional 4 h. The mixture was abandoned and supplemented with 150 $\mu$L of dimethyl sulfoxide. Finally, the plate was recorded with a microplate reader at a wavelength of 490 nm. Live/dead state detection was performed in a six-well plate. After incubation with UCNPs−BPS for 3 h, the cells were treated according to the MTT assay. One milliliter of calcein AM and PI were added and held for 1 h. Finally, the coverslips were washed with PBS and images recorded with a Leica TCS SP8 instrument.

**Hemolysis Assay of UCNPs−BPS.** Red blood cells were obtained from human blood and washed and centrifugated several times. Then, blood cells were diluted to 1:10 with a PBS solution; 0.3 mL of a diluted cell suspension was mixed with 1.2 mL of PBS (as a negative control), 1.2 mL of deionized water (as a positive control), and 1.2 mL of PBS solutions at varying concentrations of 15.6, 31.3, 62.5, 125, 250, 500, and 1000 $\mu$g/mL. The samples were shaken and held for 2 h. Finally, the mixtures were centrifuged, and the upper supernatants



DOI: 10.1021/acs.chemmater.6b01720
*Chem. Mater.* 2016, 28, 4724−4734

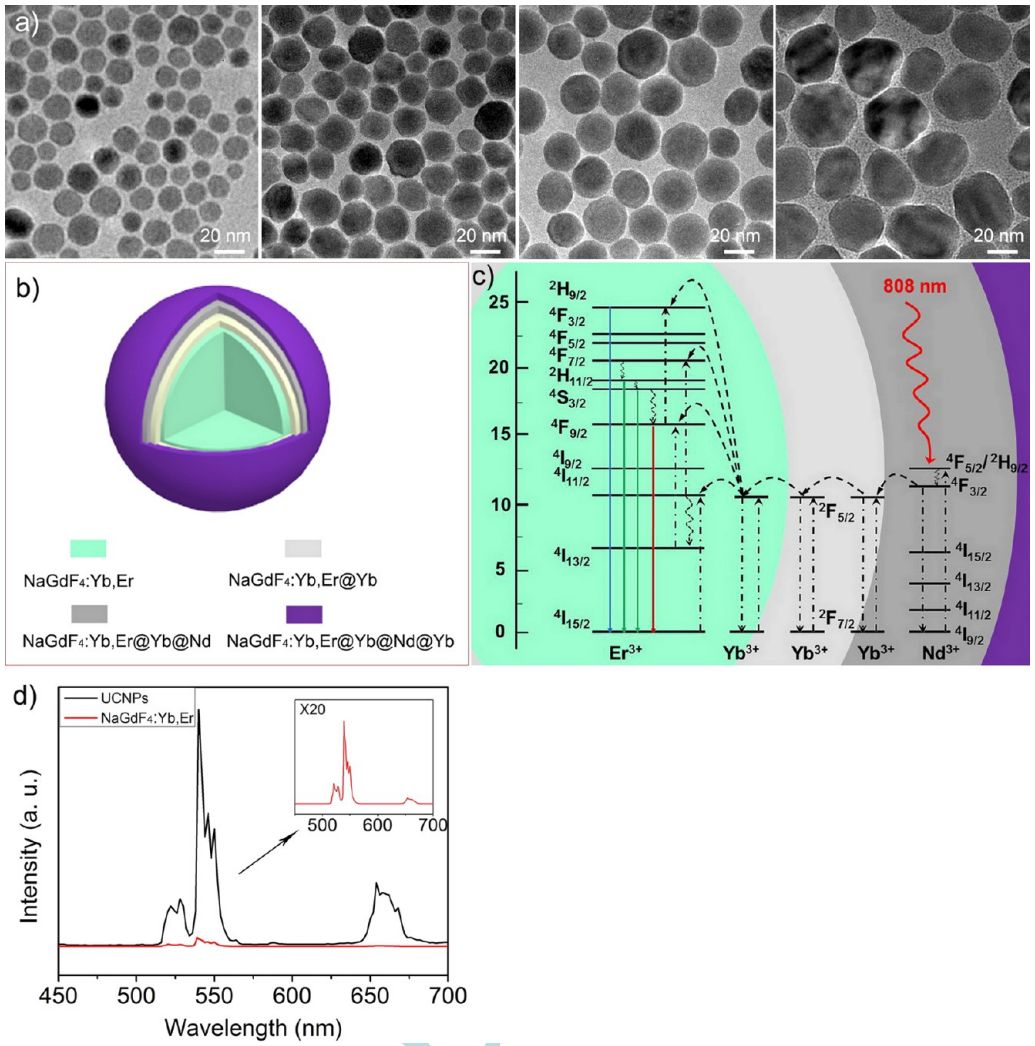


**Figure 2.** (a) TEM images of $NaGdF_4$:Yb,Er, $NaGdF_4$:Yb,Er@Yb, $NaGdF_4$:Yb,Er@Yb@Nd, and $NaGdF_4$:Yb,Er@Yb@Nb@Yb (from left to right, respectively). (b) Schematic illustration of the core−shell structure of the proposed UCNPs. (c) Proposed energy transfer mechanisms in the quenching-shield sandwich structure upon 808 nm laser excitation. (d) UCL emission spectra of the $NaGdF_4$:Yb,Er core and UCNPs.

were kept and measured by UV−vis spectroscopy to obtain the absorbance value. The hemolysis percentage was calculated by the equation hemolysis (%) = $[A_{sample} - A_{control(-)}]/[A_{control(+)} - A_{control(-)}]$, where $A$ is the absorbance.

***In Vivo* Anticancer Therapy.** Female Balb/c (25−30 g) mice were from Harbin Veterinary Research Institute of the Chinese Academy of Agricultural Sciences (Harbin, China), and all the experiments with mice were conducted in accordance with the criteria of The National Regulation of China for Care and Use of Laboratory Animals. Typically, the tumors were generated in the left axilla of each mouse by subcutaneous injection of U14 cells. After growth for the next 7 days, the tumor size was approximately 5−8 mm. Tumor-bearing mice were separated into three groups randomly: the control group without any treatment, the group under 808 nm irradiation, and the group into which UCNPs−BPS were injected under 808 nm irradiation. The irradiation pump power was 1.44 W $cm^{-2}$ for 10 min (after intravenous injection for 4 h). The mouse was injected every 2 days with 100 $\mu$L of UCNPs−BPS (1 mg $mL^{-1}$). The tumor site was irradiated every 2 days for 14 days.

**Histology Examination.** On day 14, the mice were euthanized, and representative kidney, liver, heart, lung, spleen, and tumor tissues were collected for histology analysis. The tissues were sliced and dehydrated successively and embedded in liquid paraffin. After that, the tissues were sliced to 3−5 mm for hematoxylin and eosin (H&E) staining. The final stained slices were put on the coverslips and images recorded using a Leica TCS SP8 instrument.

**Biodistribution Detection *in Vivo*.** The biodistribution of UCNPs−BPS was detected at different times after intravenous injection. Typically, Balb/c mice were injected intravenously with UCNPs−BPS (20 mg/kg dose). The mice ($n$ = 3) were euthanized at different time points (1 h, 4 h, 12 h, 24 h, 3 days, 7 days, and 14 days). The tumor and major organs (heart, liver, spleen, lung, and kidney) were collected and dissolved with 5 mL of $HNO_3$ and HCl (1:3 volume ratio) and then heated at 70 °C for 5 min to obtain clear solutions. After that, the solutions were centrifuged and the supernatant was kept for further ICP-OES analysis.

**Characterization.** Powder X-ray diffraction (XRD) measurements were performed on a Rigaku D/max TTR-III diffractometer using Cu K$\alpha$ radiation ($\lambda$ = 0.15405 nm) with a scanning rate of 15°/min in the 2$\theta$ range of 10−80°. The morphology and structure were recorded via transmission electron microscopy (TEM) (FEI Tecnai $G^2$ S-Twin). Atomic force microscope images were recorded by CSPM5500. The X-ray photoelectron spectrum was measured on a VG ESCALAB MK II electron energy spectrometer using Mg KR radiation (1253.6 eV) as the X-ray excitation source. Fourier transform infrared spectroscopy (FT-IR) spectra were recorded on a PerkinElmer 580B IR spectrophotometer using the KBr pellet as the background. UCL emission spectra were recorded on an Edinburgh FLS 980 instrument using an 808 nm laser diode controller and a 650 nm laser product


DOI: 10.1021/acs.chemmater.6b01720
Chem. Mater. 2016, 28, 4724−4734

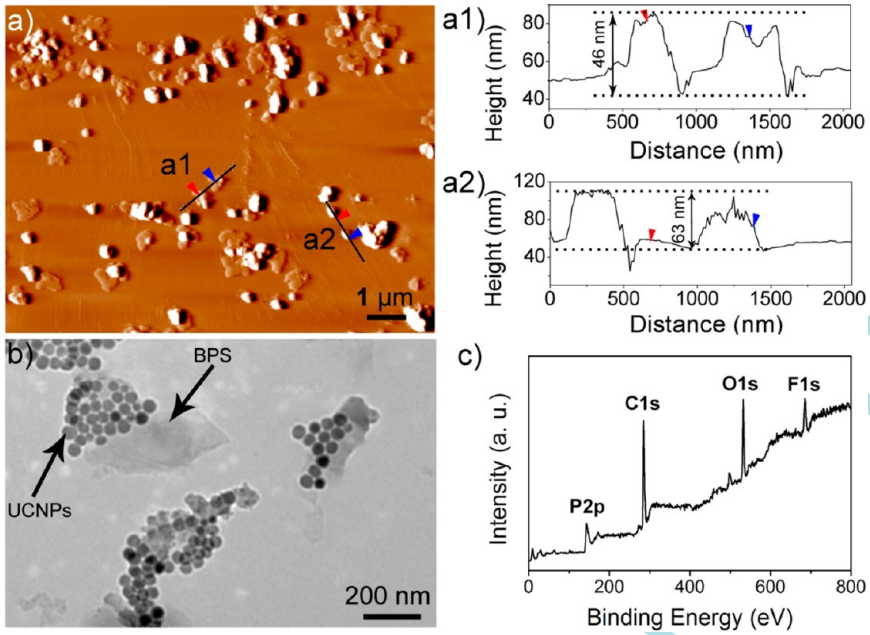


**Figure 3.** (a) AFM image of UCNPs−BPS and (a1 and a2) its height profiles along the two black lines. (b) TEM image and (c) XPS pattern of UCNPs−BPS.

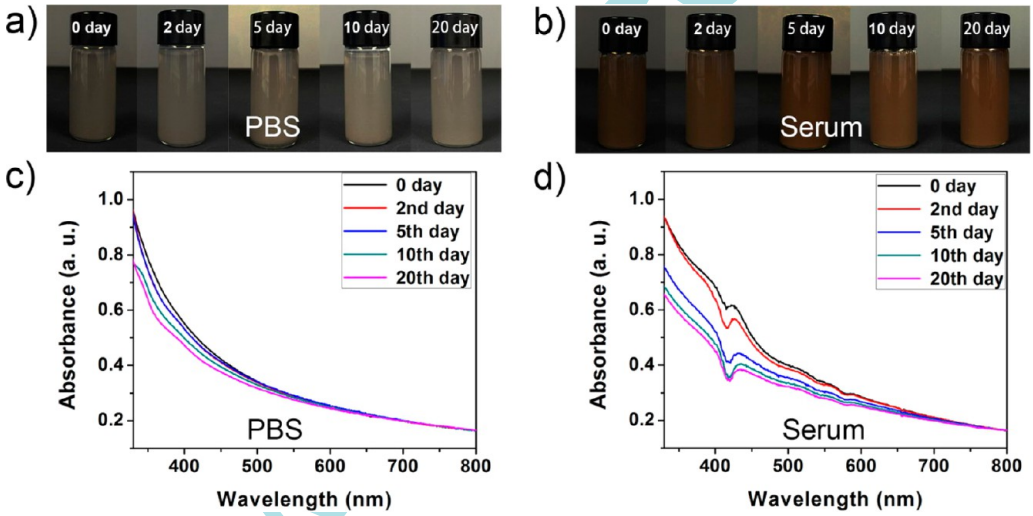


**Figure 4.** (a and b) Photographs of the solutions and (c and d) absorbance spectra at different time points of UCNPs−BPS dispersed in PBS and serum solutions.

(MW-GX-650/2000 mW) as separate laser sources. The lasers were purchased from Changchun New Industries Optoelectronics Technology Co., Ltd. All of the diode lasers are fixed wavelength with the fiber of multitransverse mode. The ultraviolet visible (UV−vis) absorbance spectra of the solutions were recorded on a UV-1601 spectrophotometer. Confocal laser scanning microscopy (CLSM) images were recorded using a Leica SP8 instrument. The UCL images were obtained on a Nikon Ti-S instrument with external 808 nm laser irradiation.

## RESULTS AND DISCUSSION

**Synthesis and Characterization of the Sample.** Scheme 1 presents an illustration of the synthesis of UCNPs−BPS, which contains two main parts: synthesis of BPS-$NH_2$ and UCNPs−PAA. The UCNPs could convert NIR light (808 nm) to visible light (green and red emission) through an upconversion energy transfer process. Meanwhile, both irradiation and emission light could donate energy to BPS to generate ROS, and the emitted green light could be utilized for diagnosis. Thus, through integration of the two parts, the UCNPs−BPS could be excited under 808 nm light for imaging-guided photodynamic therapy. Panels a and b of Figure 1 show the TEM images of black phosphorus nanosheets; the atomic force microscopy (AFM) image of BPS and its height profiles along the black lines are shown in Figure 1c. As shown, the BPS with an average height of 3 nm is very thin. The TEM images of the UCNPs synthesized at different steps are given in Figure 2a. It can be seen that the particle size gradually increases with an increase in the number of coated layers, and the shape and dispersity of the four-layer UCNPs (Figure 2b) can well be maintained with an average size of ∼50 nm.

Figure S1 shows the XRD patterns of BPS, UCNPs, and UCNPs−BPS. As depicted, the crystals of UCNPs are well assigned to the hexagonal $NaGdF_4$ (JCPDS Card No. 27-0699).



DOI: 10.1021/acs.chemmater.6b01720
Chem. Mater. 2016, 28, 4724−4734

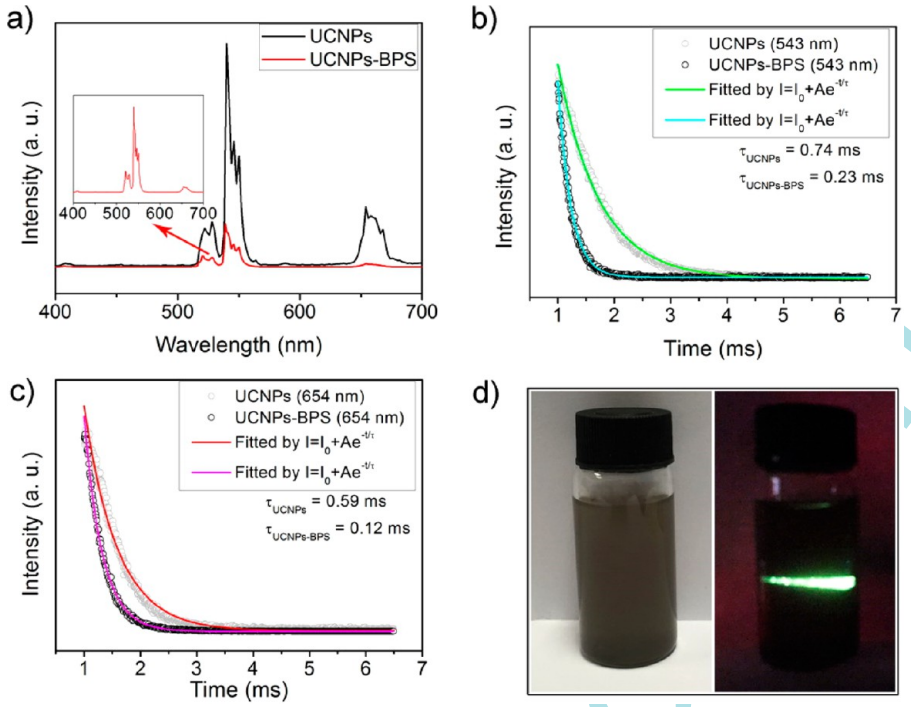


**Figure 5.** Upconversion luminescence properties of UCNPs and UCNPs−BPS. (a) UCL spectra under 808 nm laser irradiation. Decay curves at wavelengths of (b) 543 and (c) 654 nm. (d) Photographs of UCNPs−BPS in a PBS solution under daylight and under 808 nm irradiation.

In the XRD pattern of BPS, the obvious (020), (040), and (060) lattice planes indicate the typical two-dimensional (2D) sheet structure. After conjunction of UCNPs, the XRD pattern of the UCNPs−BPS complex comprises two sets of crystal lattices, the BPS and UCNPs.

The AFM image and TEM image of UCNPs−BPS further indicate that the complex maintains good dispersity (Figure 3a,b), which is also verified by the results of statistical AFM analysis given in Figure S2. As indicated, the smaller UCNPs are distributed well on the surface of BPS. The average height of the composite is 62 nm, which is basically consistent with the whole thickness of BPS (~3 nm) and UCNPs (~50 nm). The average size of the UCNPs−BPS complex is 197 nm, and the maximal size is 400 nm (Figures S2 and S3), which can be applied for further biomedical uses. The XPS spectrum of UCNPs−BPS (Figure 3c) indicates that the P, C, O, and F elements exist in the composite. All TEM, XRD, AFM, and XPS results described above confirm the successful integration of BPS and UCNPs.

When the compounds are used as potential theranostic agents, it is essential to evaluate the biostability in the stimulated body fluid, such as PBS and serum. We detected the stability of the UCNPs−BPS dispersed into the PBS solution and serum-containing medium. After the two solutions had been stirred softly at 37 °C for different times of 0, 2, 5, 10, and 20 days, the photographs of the solutions and the corresponding absorbance spectra were recorded. As shown in panels a and b of Figure 4, the samples remained stable in the two separate solutions. The absorbance intensity decreases little (Figure 4c,d) with an increase in time because of little degradation of BPS, and the absorbance exists in the whole visible region, which indicates there are 2D nanosheets.[33] On day 20, the dynamic light scattering properties reveal the UCNPs−BPS almost maintain good dispersion (Figure S4a,b), and the average diameters in the PBS solutions and serum-containing media are 190 and 295 nm, respectively. Figure S5 shows the ζ potential curves of the samples in the two media (−28.2 and −23.9 mV), indicating the sample can be stable in the PBS and serum media.

The functionalization of PAA and RGD peptide on the samples was characterized by FT-IR spectroscopy, and the corresponding spectra of UCNPs−PAA, UCNPs−BPS, and UCNPs−BPS−RGD are presented in Figure S6. As shown, the similar band in all three samples at 3345 $cm^{-1}$ is due to −OH stretching. The characteristic absorption bands of C−H (1465 $cm^{-1}$), uncharged C═O (1570 $cm^{-1}$), charged C═O (1710 $cm^{-1}$), and −CH (2940 $cm^{-1}$) in UCNPs−PAA suggest the successful linkage of PAA. Compared with UCNPs with an oleic acid coating, stronger peaks are displayed in the UCNPs−PAA, indicating uncharged carboxylic acid groups were generated and increased in frequency during the modification process. The unique absorption peaks at 1432 and 1048 $cm^{-1}$ are from $-NH_2$ and −COOR, respectively, due to the successful conjunction of PEG-$NH_2$-modified BPS. After modification with the RGD peptide finally, the unique peaks of −CO−NH− (804 $cm^{-1}$), C−O (1076 $cm^{-1}$), and −NH (1633 $cm^{-1}$) are characteristic of the RGD peptide.

To achieve the highest UC emission for more efficient PDT, we designed a four-layer core−shell $NaGdF_4$:Yb,Er@Yb@Nd@Yb structure. As expected, the UCL emission intensity of UCNPs has been dramatically increased compared with that of the $NaGdF_4$:Yb,Er core because of efficient elimination of the back energy transfer from $Er^{3+}$ to $Nd^{3+}$ by the quenching-shield $NaGdF_4$:Yb shell (Figure 2b−d). The UCL properties of UCNPs and UCNPs−BPS are given in Figure 5. In Figure 5a, the emissions at 409, 520−560, and 650−670 nm of UCNPs under 808 nm laser excitation are assigned to the respective $^2H_{9/2} \rightarrow {}^4I_{15/2}$, $^2H_{11/2}/{}^4S_{3/2} \rightarrow {}^4I_{15/2}$, and $^4F_{9/2} \rightarrow {}^4I_{15/2}$ transitions of $Er^{3+}$ ions, respectively. After modification with BPS, there is an obvious decrease in the whole emission region.



DOI: 10.1021/acs.chemmater.6b01720
Chem. Mater. 2016, 28, 4724−4734

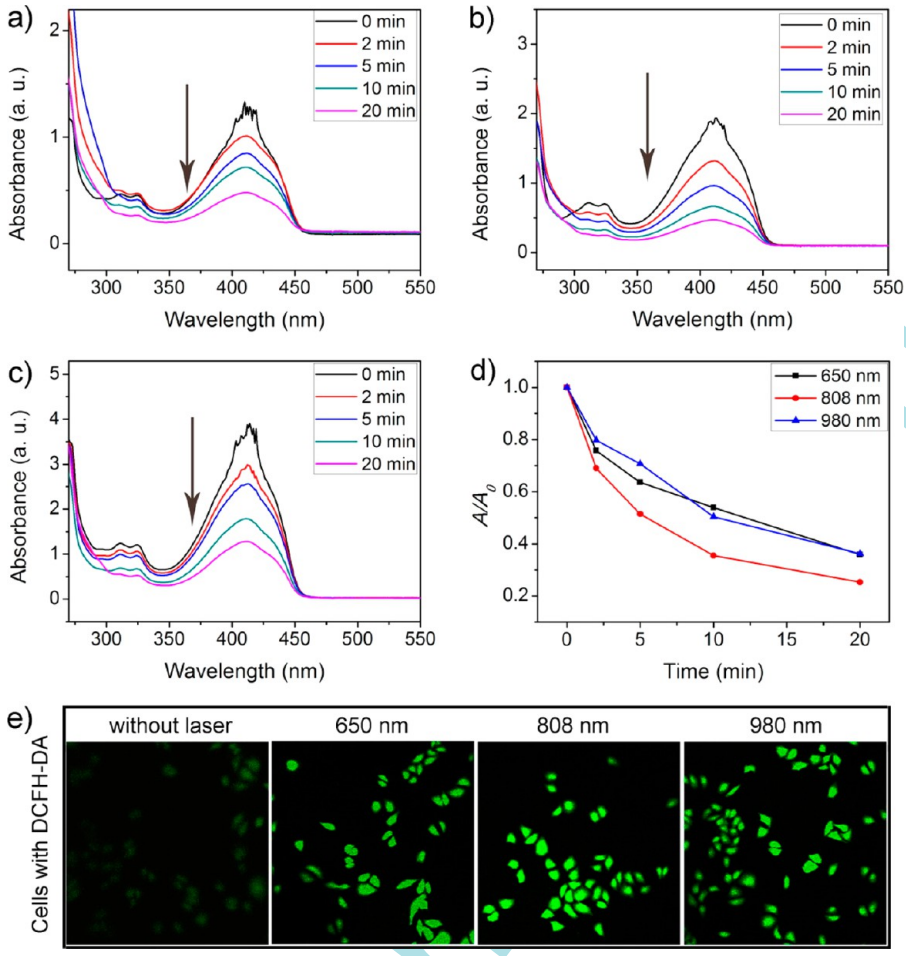


**Figure 6.** Photodynamic properties of UCNPs−BPS. The absorbance spectra of DPBF mixed with UCNPs−BPS under different lasers at wavelengths of (a) 650, (b) 808, and (c) 980 nm at different irradiation time points. (d) Normalized absorbance at a wavelength of 410 nm at different irradiation time points. (e) Confocal laser scanning microscopy images of HeLa cells with oxidized DCF fluorescence under different irradiation lasers. All the laser pump powers were 1.44 W $cm^{-2}$.

In particular, the red emission at 650 nm almost disappears, indicating the efficient energy transfer from UCNPs to BPS caused by the fluorescence resonance energy transfer (FRET) process. The decay curves at 543 nm ($^4S_{3/2} \rightarrow {}^4I_{15/2}$ transition) and 654 nm ($^4F_{9/2} \rightarrow {}^4I_{15/2}$ transition) of UCNPs and UCNPs−BPS under 808 nm laser excitation are depicted in panels b and c of Figure 5. As shown, the lifetimes of the two groups decrease from 0.74 to 0.23 ms and from 0.59 to 0.12 ms, respectively, further confirming the FRET process. Under 808 nm laser irradiation, a strong green light band can still be found for the UCNPs−BPS dispersed in the PBS solution, suggesting its possible use as a bioimaging probe (Figure 5d).

**Extracellular and Intracellular Singlet Oxygen Detection.** The photodynamic properties of the samples are examined, as presented in Figure 6. Here, a DPBF solution is utilized to evaluate the amount of ROS in the solution, and DCFH-DA was used for the *in vitro* measurement. When ROS are generated, DPBF will be oxidized, leading to the decrease in the absorbance intensity at a wavelength of 410 nm. In Figure 6a−c, when different laser sources are used, all of the absorbance intensities in the three groups decrease with a prolonged time. From the calculated curves (Figure 6d), the normalized absorbance at 20 min irradiated with wavelengths of 650, 808, and 980 nm is 35.9, 25.3, and 36.2%, respectively, indicating the 808 nm laser light can cause the largest amount of ROS. There are two reasons for this. First, the UCNPs−BPS could generate ROS under whole visible light.[33] That means the irradiations at 650 and 808 nm themselves are both effective sources for motivating the UCNPs−BPS. Meanwhile, under 808 and 980 nm irradiation, the emitted visible light in the green and red regions due to the two-photon upconversion energy transfer process is also effective. Second, the solution agents have the decreased absorbance of lasers with the irradiation wavelengths decreased from 980 to 808 nm and then to 650 nm. The 650 nm laser has the largest penetration depth in water, but the 808 nm laser has the largest penetration depth in the biofluid (hemoglobin and water). In summary, the 808 nm light has the highest rate of ROS production. Also, we detected the intracellular ROS yield using DCFH-DA. The dye of DCFH-DA could not emit fluorescence but could be taken up by cells. After hydrolysis to DCFH by intracellular esterase, the DCFH molecules that could be oxidized to DCF with strong green luminescence at an irradiation wavelength of 488 nm remain. The CLSM images of HeLa cells with oxidized DCF fluorescence are shown in Figure 6e. The relatively stronger green luminescence also shows the highest ROS generation capability of 808 nm laser light.

***In Vitro* and *In Vivo* Cytotoxicity and Imaging.** As UCNPs−BPS could generate ROS under visible light and near-infrared light, the antitumor efficiency was further detected


DOI: 10.1021/acs.chemmater.6b01720
*Chem. Mater.* 2016, 28, 4724−4734

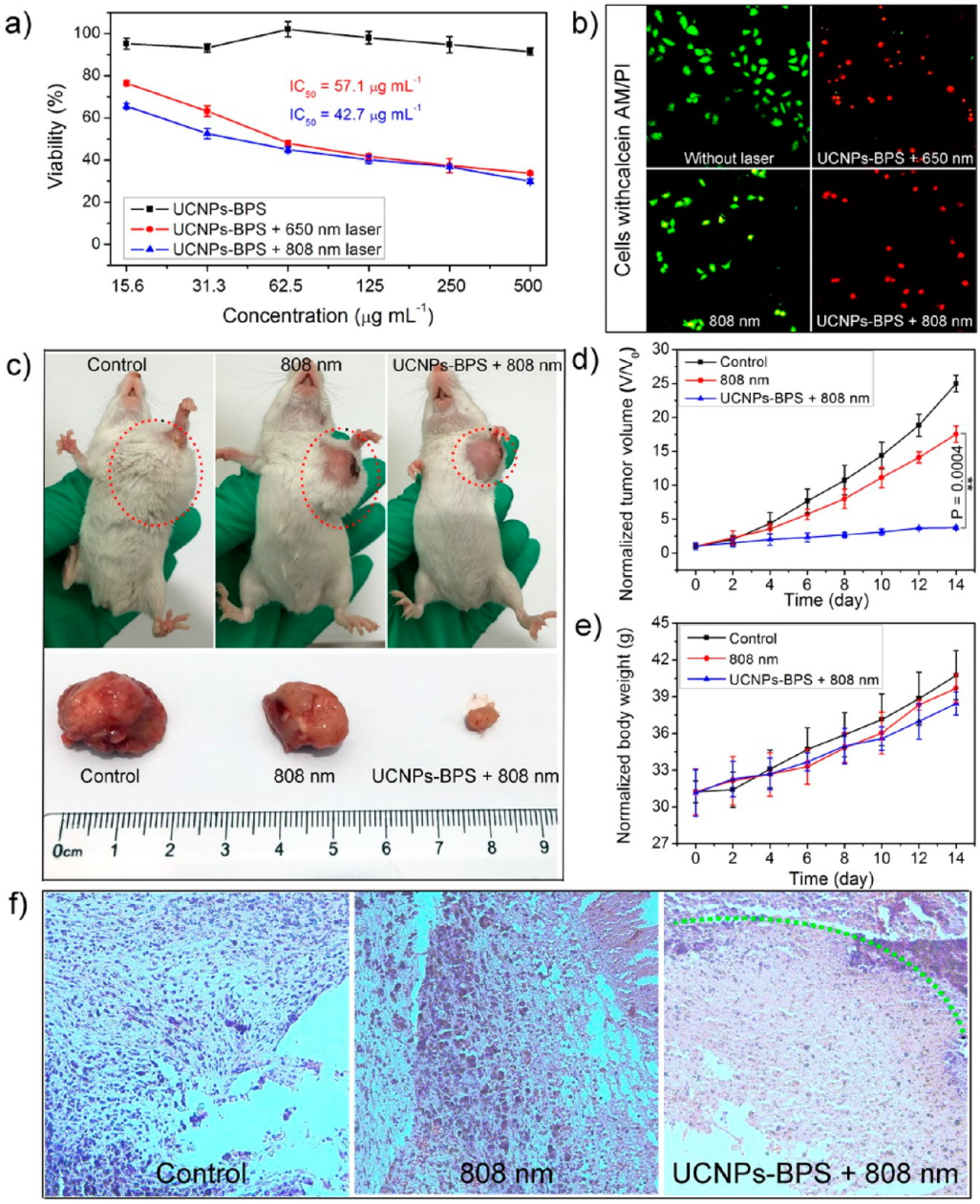


**Figure 7.** (a) Viability of HeLa cells incubated with UCNPs−BPS under different laser conditions using the MTT assay. (b) Corresponding microscopy images marked with calcein AM/PI. (c) Photographs of mice and tumors on day 14. (d) Body weight and (e) tumor volume with prolonged times. (f) H&E-stained images of the tumors from different groups.

against HeLa cells *in vitro* and *in vivo*. The uptake by cells of the UCNP−BPS nanoparticles was first examined. As shown in Figure S7, the red fluorescence arising from the material itself is enhanced with an increase in incubation time from 0.5 to 3 h. Meanwhile, under 808 nm light irradiation, the cells can emit bright green light, which can be used for imaging to track the carrier and diagnose tumor position (Figure S8). In Figure 7a, after incubation with UCNPs−BPS without irradiation, the viability of cells remained high (91.5−102.1%), indicating that UCNPs−BPS are weakly toxic to cells. When samples were irradiated with 650 and 808 nm light, there was a concentration-dependent cytotoxicity with viabilities of 33.7−76.5 and 29.8−65.6%, respectively, and the corresponding $IC_{50}$ values were 57.1 and 42.7 $\mu$g mL$^{-1}$, respectively, indicating the high anticancer efficiency. This result could also be vividly proven by the live/dead states of different treatment groups (Figure 7b). It is noted that low toxicity to cells is detected for 808 nm laser irradiation alone, indicating the 808 nm laser light has no obvious side effects on cells and tissues.

To be applied *in vivo*, the *in vivo* biocompatibility and biodistribution should be clarified first. The result of hemolysis of the sample using human red blood cells is shown in Figure S9a. In water, the red solution is caused by the presence of hemoglobin separated from red cells in the water (inset of Figure S9a). No visually red color is found in the PBS solutions mixed with UCNPs−BPS with varied concentration from 15.6 to 1000 $\mu$g/mL. The highest hemolytic value of UCNPs−BPS is 0.91%, indicating almost no hemolysis occurs. The good compatibility of UCNPs−BPS with blood suggests the samples can be potentially used in live cells. The biodistribution of


DOI: 10.1021/acs.chemmater.6b01720
Chem. Mater. 2016, 28, 4724−4734

UCNPs−BPS with different times after intravenous injection was detected by ICP-OES. As shown in Figure S9b, there is little accumulation in the whole stage in the heart and kidney, and the amount of the Gd element decreases in all organs and tumor with increased time. In the early stages (1 h, 4 h, 12 h, and 1 day), the Gd element mainly appears in the liver, spleen, and lung. Meanwhile, the particles could be targeted to the tumors because of the targeted RGD peptide. On days 7 and 14 after injection, the particles in the liver, spleen, lung, and tumor are much smaller than those on the first day. The results reveal that the injected UCNPs−BPS can be excreted from the mice with prolonged times.

The *in vivo* antitumor performance was further examined. The tumor-bearing mice are divided into three groups: the blank group as control, the groups treated with pure 808 nm irradiation, and UCNPs−BPS with 808 nm light irradiation. After being treated with different conditions every 2 days for 14 days, the mice and tumors from different groups are shown in Figure 7c. As shown, UCNPs−BPS with 808 nm light irradiation show the strongest tumor inhibition effect, while pure 808 nm NIR light has a negligible effect on the therapy, which is quite consistent with the *in vitro* results. In Figure 7d, the tumor sizes decrease from the first group to the third. In the third group, the tumors are almost inhibited, also indicating the high anticancer efficiency of UCNPs−BPS under 808 nm light irradiation. Meanwhile, the body weights continue to increase, showing there is no side effect of UCNPs−BPS (Figure 7e). The H&E-stained images of tumors from different groups reveal that UCNPs−BPS under 808 nm light irradiation can efficiently kill the cells and induce apoptosis (Figure 7f). The H&E-stained images of the tissues (heart, liver, spleen, lung, and kidney) from different groups are presented in Figure S10. There are no abnormal phenomena in the third group: no damage is found in the hepatocytes, no fibrosis appears in the pulmonary, and no concentration is observed in the glomerulus. All the *in vitro* and *in vivo* results evidently demonstrate the potential applicability of UCNPs−BPS as an antitumor agent under a single 808 nm irradiation.

## CONCLUSIONS

In summary, a novel UCNPs−BPS composite composed of ultrathin black phosphorus nanosheets and the small $NaGdF_4$:Yb,Er@Yb@Nd@Yb UCNPs was first fabricated for 808 nm excited photodynamic therapy. Upon 808 nm NIR light irradiation, the UCNPs−BPS composite has ROS generation capability greater than those of 650 and 980 nm irradiations, resulting in enhanced anticancer properties, as verified by *in vitro* and *in vivo* results. Meanwhile, the emitted green light could be used for diagnosis.

## ASSOCIATED CONTENT

### Supporting Information

The Supporting Information is available free of charge on the ACS Publications website at DOI: 10.1021/acs.chemmater.6b01720.

XRD patterns of as-synthesized samples; statistical AFM analysis, diameter distribution, and height distribution of UCNPs−BPS; AFM image of UCNPs−BPS; dynamic light scattering properties of UCNPs−BPS dispersed in PBS and serum solutions; FT-IR spectra of the as-synthesized samples; $\zeta$ potential curves of UCNPs−BPS dispersed in PBS and serum; confocal laser scanning microscopy images of HeLa cells with UCNPs−BPS taken up with prolonged incubation times; inverted fluorescence microscopy images of HeLa cells incubated with UCNPs−BPS; hemolysis properties of human red blood cells; the biodistribution in the organs and tumors after intravenous injection of UCNPs−BPS; and H&E-stained images of the tissues in the three groups (PDF)

## AUTHOR INFORMATION

### Corresponding Authors

*E-mail: yangpiaoping@hrbeu.edu.cn.
*E-mail: jlin@ciac.ac.cn.

### Notes

The authors declare no competing financial interest.

## ACKNOWLEDGMENTS

Financial support from the Natural Science Foundation of China (NSFC 21271053, 21401032, 51472058, 51332008, and 51502050), the Outstanding Youth Foundation of Heilongjiang Province (JC2015003), and the Fundamental Research funds for the Central Universities is gratefully acknowledged.

## REFERENCES

(1) Chen, H. M.; Wang, G. D.; Chuang, Y. J.; Zhen, Z. P.; Chen, X. Y.; Biddinger, P.; Hao, Z. L.; Liu, F.; Shen, B. Z.; Pan, Z. W.; Xie, J. Nanoscintillator-Mediated X-ray Inducible Photodynamic Therapy for *In Vivo* Cancer Treatment. *Nano Lett.* **2015**, *15*, 2249−2256.

(2) Jayakumar, M. K. G.; Bansal, A.; Huang, K.; Yao, R.; Li, B. N.; Zhang, Y. Near-Infrared-Light-Based NanoPlatform Boosts Endosomal Escape and Controls Gene Knockdown *in Vivo*. *ACS Nano* **2014**, *8*, 4848−4858.

(3) Zhang, C.; Zhao, K.; Bu, W.; Ni, D.; Liu, Y.; Feng, J.; Shi, J. Marriage of Scintillator and Semiconductor for Synchronous Radiotherapy and Deep Photodynamic Therapy with Diminished Oxygen Dependence. *Angew. Chem., Int. Ed.* **2015**, *54*, 1770−1774.

(4) Wang, Y.; Song, S.; Liu, J.; Liu, D.; Zhang, H. ZnO-Functionalized Upconverting Nanotheranostic Agent: Multi-Modality Imaging-Guided Chemotherapy with On-Demand Drug Release Triggered by pH. *Angew. Chem., Int. Ed.* **2015**, *54*, 536−540.

(5) Kim, J.; Piao, Y.; Hyeon, T. Multifunctional Nanostructured Materials for Multimodal Imaging, and Simultaneous Imaging and Therapy. *Chem. Soc. Rev.* **2009**, *38*, 372−390.

(6) Castano, A. P.; Mroz, P.; Hamblin, M. R. Photodynamic Therapy and Anti-tumour Immunity. *Nat. Rev. Cancer* **2006**, *6*, 535−545.

(7) Kalluru, P.; Vankayala, R.; Chiang, C.-S.; Hwang, K. C. Photosensitization of Singlet Oxygen and *In Vivo* Photodynamic Therapeutic Effects Mediated by PEGylated $W_{18}O_{49}$ Nanowires. *Angew. Chem., Int. Ed.* **2013**, *52*, 12332−12336.

(8) Seidl, C.; Ungelenk, J.; Zittel, E.; Bergfeldt, T.; Sleeman, J. P.; Schepers, U.; Feldmann, C. Tin Tungstate Nanoparticles: A Photosensitizer for Photodynamic Tumor Therapy. *ACS Nano* **2016**, *10*, 3149−3157.

(9) Wang, X.; Liu, K.; Yang, G.; Cheng, L.; He, L.; Liu, Y.; Li, Y.; Guo, L.; Liu, Z. Near-infrared Light Triggered Photodynamic Therapy in Combination with Gene Therapy Using Upconversion Nanoparticles for Effective Cancer Cell Killing. *Nanoscale* **2014**, *6*, 9198−9205.

(10) Turan, I. S.; Yildiz, D.; Turksoy, A.; Gunaydin, G.; Akkaya, E. U. A Bifunctional Photosensitizer for Enhanced Fractional Photodynamic Therapy: Singlet Oxygen Generation in the Presence and Absence of Light. *Angew. Chem., Int. Ed.* **2016**, *55*, 2875−2878.

(11) Liu, K.; Xing, R.; Zou, Q.; Ma, G.; Mohwald, H.; Yan, X. Simple Peptide-Tuned Self-Assembly of Photosensitizers towards Anticancer Photodynamic Therapy. *Angew. Chem., Int. Ed.* **2016**, *55*, 3036−3039.





DOI: 10.1021/acs.chemmater.6b01720
*Chem. Mater.* 2016, 28, 4724−4734

(12) Chatterjee, D. K.; Fong, L. S.; Zhang, Y. Nanoparticles in Photodynamic Therapy: An Emerging Paradigm. *Adv. Drug Delivery Rev.* **2008**, *60*, 1627−1637.
(13) Liu, Y.; Liu, Y.; Bu, W.; Cheng, C.; Zuo, C.; Xiao, Q.; Sun, Y.; Ni, D.; Zhang, C.; Liu, J.; Shi, J. Hypoxia Induced by Upconversion-Based Photodynamic Therapy: Towards Highly Effective Synergistic Bioreductive Therapy in Tumors. *Angew. Chem., Int. Ed.* **2015**, *54*, 8105−8109.
(14) Wang, C.; Cheng, L.; Liu, Y.; Wang, X.; Ma, X.; Deng, Z.; Li, Y.; Liu, Z. Imaging-Guided pH-Sensitive Photodynamic Therapy Using Charge Reversible Upconversion Nanoparticles under Near-Infrared Light. *Adv. Funct. Mater.* **2013**, *23*, 3077−3086.
(15) Im, H.; Kim, S.; Park, C.; Jang, S.-H.; Kim, C.-J.; Kim, K.; Park, N.-G.; Kim, C. High Performance Organic Photosensitizers for Dye-Sensitized Solar Cells. *Chem. Commun.* **2010**, *46*, 1335−1337.
(16) Roy, I.; Ohulchanskyy, T. Y.; Pudavar, H. E.; Bergey, E. J.; Oseroff, A. R.; Morgan, J.; Dougherty, T. J.; Prasad, P. N. Ceramic-Based Nanoparticles Entrapping Water-Insoluble Photosensitizing Anticancer Drugs: A Novel Drug−Carrier System for Photodynamic Therapy. *J. Am. Chem. Soc.* **2003**, *125*, 7860−7865.
(17) Ohulchanskyy, T. Y.; Roy, I.; Goswami, L. N.; Chen, Y.; Bergey, E. J.; Pandey, R. K.; Oseroff, A. R.; Prasad, P. N. Organically Modified Silica Nanoparticles with Covalently Incorporated Photosensitizer for Photodynamic Therapy of Cancer. *Nano Lett.* **2007**, *7*, 2835−2842.
(18) Lv, R.; Zhong, C.; Li, R.; Yang, P.; He, F.; Gai, S.; Hou, Z.; Yang, G.; Lin, J. Multifunctional Anticancer Platform for Multimodal Imaging and Visible Light Driven Photodynamic/Photothermal Therapy. *Chem. Mater.* **2015**, *27*, 1751−1763.
(19) Lucky, S. S.; Muhammad Idris, N.; Li, Z.; Huang, K.; Soo, K. C.; Zhang, Y. Titania Coated Upconversion Nanoparticles for Near-Infrared Light Triggered Photodynamic Therapy. *ACS Nano* **2015**, *9*, 191−205.
(20) Noimark, S.; Weiner, J.; Noor, N.; Allan, E.; Williams, C. K.; Shaffer, M. S. P.; Parkin, I. P. Dual-Mechanism Antimicrobial Polymer-ZnO Nanoparticle and Crystal Violet-Encapsulated Silicone. *Adv. Funct. Mater.* **2015**, *25*, 1367−1373.
(21) Zhang, X.; Wang, H.; Wang, H.; Zhang, Q.; Xie, J.; Tian, Y.; Wang, J.; Xie, Y. Single-Layered Graphitic-C3N4 Quantum Dots for Two-Photon Fluorescence Imaging of Cellular Nucleus. *Adv. Mater.* **2014**, *26*, 4438−4443.
(22) Yu, Z.; Sun, Q.; Pan, W.; Li, N.; Tang, B. A Near-Infrared Triggered Nanophotosensitizer Inducing Domino Effect on Mitochondrial Reactive Oxygen Species Burst for Cancer Therapy. *ACS Nano* **2015**, *9*, 11064−11074.
(23) Woomer, A. H.; Farnsworth, T. W.; Hu, J.; Wells, R. A.; Donley, C. L.; Warren, S. C. Phosphorene: Synthesis, Scale-Up, and Quantitative Optical Spectroscopy. *ACS Nano* **2015**, *9*, 8869−8884.
(24) Li, L. K.; Yu, Y. J.; Ye, G. J.; Ge, Q. Q.; Ou, X. D.; Wu, H.; Feng, D. L.; Chen, X. H.; Zhang, Y. B. Black Phosphorus Field-Effect Transistors. *Nat. Nanotechnol.* **2014**, *9*, 372−377.
(25) Qiao, J. S.; Kong, X. H.; Hu, Z. X.; Yang, F.; Ji, W. High-Mobility Transport Anisotropy and Linear Dichroism in Few-Layer Black Phosphorus. *Nat. Commun.* **2014**, *5*, 4475.
(26) Xia, F. N.; Wang, H.; Jia, Y. C. Rediscovering Black Phosphorus as an Anisotropic Layered Material for Optoelectronics and Electronics. *Nat. Commun.* **2014**, *5*, 4458.
(27) Engel, M.; Steiner, M.; Avouris, P. Black Phosphorus Photodetector for Multispectral, High-Resolution Imaging. *Nano Lett.* **2014**, *14*, 6414−6417.
(28) Fei, R.; Yang, L. Strain-Engineering the Anisotropic Electrical Conductance of Few-Layer Black Phosphorus. *Nano Lett.* **2014**, *14*, 2884−2889.
(29) Yasaei, P.; Kumar, B.; Foroozan, T.; Wang, C.; Asadi, M.; Tuschel, D.; Indacochea, J. E.; Klie, R. F.; Salehi-Khojin, A. High-Quality Black Phosphorus Atomic Layers by Liquid-Phase Exfoliation. *Adv. Mater.* **2015**, *27*, 1887−1892.
(30) Li, L.; Yu, Y.; Ye, G. J.; Ge, Q.; Ou, X.; Wu, H.; Feng, D.; Chen, X. H.; Zhang, Y. Black Phosphorus Field-effect Transistors. *Nat. Nanotechnol.* **2014**, *9*, 372−377.
(31) Kang, J.; Wood, J. D.; Wells, S. A.; Lee, J.-H.; Liu, X.; Chen, K.-S.; Hersam, M. C. Solvent Exfoliation of Electronic-Grade, Two-Dimensional Black Phosphorus. *ACS Nano* **2015**, *9*, 3596−3604.
(32) Hanlon, D.; Backes, C.; Doherty, E.; Cucinotta, C. S.; Berner, N. C.; Boland, C.; Lee, K.; Harvey, A.; Lynch, P.; Gholamvand, Z.; Zhang, S.; Wang, K.; Moynihan, G.; Pokle, A.; Ramasse, Q. M.; McEvoy, N.; Blau, W. J.; Wang, J.; Abellan, G.; Hauke, F.; Hirsch, A.; Sanvito, S.; O'Regan, D. D.; Duesberg, G. S.; Nicolosi, V.; Coleman, J. N. Liquid Exfoliation Of Solvent-Stabilized Few-Layer Black Phosphorus for Applications Beyond Electronics. *Nat. Commun.* **2015**, *6*, 8563.
(33) Wang, H.; Yang, X.; Shao, W.; Chen, S.; Xie, J.; Zhang, X.; Wang, J.; Xie, Y. Ultrathin Black Phosphorus Nanosheets for Efficient Singlet Oxygen Generation. *J. Am. Chem. Soc.* **2015**, *137*, 11376−11382.
(34) Sun, Z.; Xie, H.; Tang, S.; Yu, X.-F.; Guo, Z.; Shao, J.; Zhang, H.; Huang, H.; Wang, H.; Chu, P. K. Ultrasmall Black Phosphorus Quantum Dots: Synthesis and Use as Photothermal Agents. *Angew. Chem., Int. Ed.* **2015**, *54*, 11526−11530.
(35) Sun, L.-D.; Wang, Y.-F.; Yan, C.-H. Paradigms and Challenges for Bioapplication of Rare Earth Upconversion Luminescent Nanoparticles: Small Size and Tunable Emission/Excitation Spectra. *Acc. Chem. Res.* **2014**, *47*, 1001−1009.
(36) Wang, G.; Peng, Q.; Li, Y. Lanthanide-Doped Nanocrystals: Synthesis, Optical-Magnetic Properties, and Applications. *Acc. Chem. Res.* **2011**, *44*, 322−332.
(37) Lv, R.; Yang, P.; He, F.; Gai, S.; Li, C.; Dai, Y.; Yang, G.; Lin, J. A Yolk-like Multifunctional Platform for Multimodal Imaging and Synergistic Therapy Triggered by a Single Near-Infrared Light. *ACS Nano* **2015**, *9*, 1630−1647.
(38) Wang, Y.; Liu, K.; Liu, X.; Dohnalová, K.; Gregorkiewicz, T.; Kong, X.; Aalders, M. C. G.; Buma, W. J.; Zhang, H. Critical Shell Thickness of Core/Shell Upconversion Luminescence Nanoplatform for FRET Application. *J. Phys. Chem. Lett.* **2011**, *2*, 2083−2088.
(39) Liu, K.; Liu, X.; Zeng, Q.; Zhang, Y.; Tu, L.; Liu, T.; Kong, X.; Wang, Y.; Cao, F.; Lambrechts, S. A. G.; Aalders, M. C. G.; Zhang, H. Covalently Assembled NIR Nanoplatform for Simultaneous Fluorescence Imaging and Photodynamic Therapy of Cancer Cells. *ACS Nano* **2012**, *6*, 4054−4062.
(40) Li, Y.; Tang, J.; Pan, D.-X.; Sun, L.-D.; Chen, C.; Liu, Y.; Wang, Y.-F.; Shi, S.; Yan, C.-H. A Versatile Imaging and Therapeutic Platform Based on Dual-Band Luminescent Lanthanide Nanoparticles toward Tumor Metastasis Inhibition. *ACS Nano* **2016**, *10*, 2766−2773.
(41) Hao, J. H.; Zhang, Y.; Wei, X. H. Electric-Induced Enhancement and Modulation of Upconversion Photoluminescence in Epitaxial $BaTiO_3$:Yb/Er Thin Films. *Angew. Chem., Int. Ed.* **2011**, *50*, 6876−6880.
(42) Chen, G. Y.; Agren, H.; Ohulchanskyy, T. Y.; Prasad, P. N. Light Upconverting Core-Shell Nanostructures: Nanophotonic Control for Emerging Applications. *Chem. Soc. Rev.* **2015**, *44*, 1680−1713.
(43) Zheng, W.; Huang, P.; Tu, D.; Ma, E.; Zhu, H.; Chen, X. Lanthanide-doped Upconversion Nano-Bioprobes: Electronic Structures, Optical Properties, and Biodetection. *Chem. Soc. Rev.* **2015**, *44*, 1379−1415.
(44) Liu, X.; Yan, C.-H.; Capobianco, J. A. Photon Upconversion Nanomaterials. *Chem. Soc. Rev.* **2015**, *44*, 1299−1301.
(45) Zhou, J.; Liu, Q.; Feng, W.; Sun, Y.; Li, F. Upconversion Luminescent Materials: Advances and Applications. *Chem. Rev.* **2015**, *115*, 395−465.
(46) Idris, N. M.; Gnanasammandhan, M. K.; Zhang, J.; Ho, P. C.; Mahendran, R.; Zhang, Y. *In vivo* Photodynamic Therapy using Upconversion Nanoparticles as Remote-Controlled Nanotransducers. *Nat. Med.* **2012**, *18*, 1580−U190.
(47) Min, Y.; Li, J.; Liu, F.; Yeow, E. K. L.; Xing, B. Near-Infrared Light-Mediated Photoactivation of a Platinum Antitumor Prodrug and Simultaneous Cellular Apoptosis Imaging by Upconversion-Luminescent Nanoparticles. *Angew. Chem., Int. Ed.* **2014**, *53*, 1012−1016.
(48) Bogdan, N.; Vetrone, F.; Ozin, G. A.; Capobianco, J. A. Synthesis of Ligand-Free Colloidally Stable Water Dispersible Brightly




DOI: 10.1021/acs.chemmater.6b01720
*Chem. Mater.* 2016, 28, 4724−4734

Luminescent Lanthanide-Doped Upconverting Nanoparticles. *Nano Lett.* **2011**, *11*, 835−840.
(49) Gorris, H. H.; Wolfbeis, O. S. Photon-Upconverting Nanoparticles for Optical Encoding and Multiplexing of Cells, Biomolecules, and Microspheres. *Angew. Chem., Int. Ed.* **2013**, *52*, 3584−3600.
(50) Zeng, S.; Yi, Z.; Lu, W.; Qian, C.; Wang, H.; Rao, L.; Zeng, T.; Liu, H.; Liu, H.; Fei, B.; Hao, J. Simultaneous Realization of Phase/Size Manipulation, Upconversion Luminescence Enhancement, and Blood Vessel Imaging in Multifunctional Nanoprobes Through Transition Metal $Mn^{2+}$ Doping. *Adv. Funct. Mater.* **2014**, *24*, 4051−4059.
(51) Yang, Y.; Shao, Q.; Deng, R.; Wang, C.; Teng, X.; Cheng, K.; Cheng, Z.; Huang, L.; Liu, Z.; Liu, X.; Xing, B. *In Vitro* and *In Vivo* Uncaging and Bioluminescence Imaging by Using Photocaged Upconversion Nanoparticles. *Angew. Chem., Int. Ed.* **2012**, *51*, 3125−3129.
(52) Gai, S.; Li, C.; Yang, P.; Lin, J. Recent Progress in Rare Earth Micro/Nanocrystals: Soft Chemical Synthesis, Luminescent Properties, and Biomedical Applications. *Chem. Rev.* **2014**, *114*, 2343−2389.
(53) Xie, X.; Gao, N.; Deng, R.; Sun, Q.; Xu, Q.-H.; Liu, X. Mechanistic Investigation of Photon Upconversion in $Nd^{3+}$-Sensitized Core-Shell Nanoparticles. *J. Am. Chem. Soc.* **2013**, *135*, 12608−12611.
(54) Zhong, Y.; Tian, G.; Gu, Z.; Yang, Y.; Gu, L.; Zhao, Y.; Ma, Y.; Yao, J. Elimination of Photon Quenching by a Transition Layer to Fabricate a Quenching-Shield Sandwich Structure for 800 nm Excited Upconversion Luminescence of $Nd^{3+}$-Sensitized Nanoparticles. *Adv. Mater.* **2014**, *26*, 2831−2837.
(55) Wang, D.; Xue, B.; Kong, X.; Tu, L.; Liu, X.; Zhang, Y.; Chang, Y.; Luo, Y.; Zhao, H.; Zhang, H. 808 nm Driven $Nd^{3+}$-Sensitized Upconversion Nanostructures for Photodynamic Therapy and Simultaneous Fluorescence Imaging. *Nanoscale* **2015**, *7*, 190−197.
(56) He, F.; Yang, G.; Yang, P.; Yu, Y.; Lv, R.; Li, C.; Dai, Y.; Gai, S.; Lin, J. A New Single 808 nm NIR Light-Induced Imaging-Guided Multifunctional Cancer Therapy Platform. *Adv. Funct. Mater.* **2015**, *25*, 3966−3976.
(57) Lin, H.; Yu, T.; Tsang, M.-K.; Bai, G.; Zhang, Q.; Hao, J. Near-Infrared-to-Near-Infrared Down-Shifting and Upconversion Luminescence of $KY_3F_{10}$ with Single Dopant of $Nd^{3+}$ Ion. *Appl. Phys. Lett.* **2016**, *108*, 041902.
(58) Wu, M.; Congreve, D. N.; Wilson, M. W. B.; Jean, J.; Geva, N.; Welborn, M.; Van Voorhis, T.; Bulovic, V.; Bawendi, M. G.; Baldo, M. A. Solid-State Infrared-to-Visible Upconversion Sensitized by Colloidal Nanocrystals. *Nat. Photonics* **2015**, *10*, 31−34.
(59) Xiang, H.-J.; Deng, Q.; An, L.; Guo, M.; Yang, S.-P.; Liu, J.-G. Tumor Cell Specific and Lysosome-Targeted Delivery of Nitric Oxide for Enhanced Photodynamic Therapy Triggered by 808 nm Near-Infrared Light. *Chem. Commun.* **2016**, *52*, 148−151.
(60) Chen, G.; Shen, J.; Ohulchanskyy, T. Y.; Patel, N. J.; Kutikov, A.; Li, Z.; Song, J.; Pandey, R. K.; Agren, H.; Prasad, P. N.; Han, G. (alpha-$NaYbF_4$:$Tm^{3+}$)/$CaF_2$ Core/Shell Nanoparticles with Efficient Near-Infrared to Near-Infrared Upconversion for High-Contrast Deep Tissue Bioimaging. *ACS Nano* **2012**, *6*, 8280−8287.
(61) Chen, G. Y.; Ohulchanskyy, T. Y.; Liu, S.; Law, W. C.; Wu, F.; Swihart, M. T.; Agren, H.; Prasad, P. N. Core/Shell $NaGdF_4$:$Nd^{3+}$/$NaGdF_4$ Nanocrystals with Efficient Near-Infrared to Near-Infrared Downconversion Photoluminescence for Bioimaging Applications. *ACS Nano* **2012**, *6*, 2969−2977.
(62) Wang, Y.-F.; Liu, G.-Y.; Sun, L.-D.; Xiao, J.-W.; Zhou, J.-C.; Yan, C.-H. $Nd^{3+}$-Sensitized Upconversion Nanophosphors: Efficient *In Vivo* Bioimaging Probes with Minimized Heating Effect. *ACS Nano* **2013**, *7*, 7200−7206.
(63) Yang, G.; Yang, D.; Yang, P.; Lv, R.; Li, C.; Zhong, C.; He, F.; Gai, S.; Lin, J. A Single 808 nm Near-Infrared Light-Mediated Multiple Imaging and Photodynamic Therapy Based on Titania Coupled Upconversion Nanoparticles. *Chem. Mater.* **2015**, *27*, 7957−7968.
(64) Liu, B.; Chen, Y. Y.; Li, C. X.; He, F.; Hou, Z. Y.; Huang, S. S.; Zhu, H. M.; Chen, X. Y.; Lin, J. Poly(Acrylic Acid) Modification of $Nd^{3+}$-Sensitized Upconversion Nanophosphors for Highly Efficient UCL Imaging and pH-Responsive Drug Delivery. *Adv. Funct. Mater.* **2015**, *25*, 4717−4729.





DOI: 10.1021/acs.chemmater.6b01720
*Chem. Mater.* 2016, 28, 4724−4734